Surface or Bulk? Real-time Manganese Dissolution Detection in a Lithium-ion Cathode

Shahin Nikman,[1] Dongni Zhao,[1] Violeta Gonzalez-Perez,[1,2]

Harry E. Hoster[1] and Stijn F. L. Mertens[1] *

[1]Department of Chemistry, Energy Lancaster and Materials Science Institute,

Lancaster University, Bailrigg, LA1 4YW, UK

[2]Centro de Investigación Avanzada en Física Fundamental (CIAFF) and

Departamento de Física Teórica, Universidad Autónoma de Madrid

28049 Madrid, Spain

* corresponding author: s.mertens@lancaster.ac.uk; stmerten@gmail.com

Abstract

The longevity of lithium-ion batteries is determined by the rate of chemical and electrochemical side reactions that limit their charge storage capacity. In particular, dissolution of transition metals from the cathode accelerates the blockage of Li_xC_6 anodes, but few direct dissolution studies have been made to date. Although $LiMn_2O_4$ (LMO) has been frequently used as a model electrode for dissolution studies, the cause and nature of dissolution and dissolution-free states are still unclear. By online inductively coupled plasma analysis, we detect dissolution from LMO electrodes in real time to reveal the role of surface versus bulk structure effects, electrode potential and degree of lithiation on Mn dissolution. We find that fully lithiated LMO, with an average Mn redox state of 3.5, readily dissolves

when brought in contact with 0.2M Li_2SO_4, but that on initial charging a dissolution–passivation event preceding delithiation abruptly stops further detectable dissolution, until well past fully delithiated λ-MnO_2. Dissolution reactivates on returning to the initial potential of pristine LMO, and increases exponentially in the overlithiation region. Our results provide access to much more detailed dissolution information than post-mortem battery analysis allows, enabling targeted materials screening and informing best practices in charging/discharging profiles. In particular, our data suggests that suitable potential conditioning of electrodes may mitigate dissolution, as an alternative or additional measure to the use of protective surface films or incorporation of dopants.

Introduction

Lithium-ion batteries have enabled a societal revolution since their entry to market in 1991[1]. Since then, incremental advances in capacity retention, power delivery capabilities and competitive pricing have permitted their implementation in consumer electronics, vehicles and intermittent grid storage[2]. In 2018 the global energy output was 162820 TWh[3], and is estimated to grow by 27% by 2040. However, the current deployed energy storage facilities amount to only 17 GWh, while the predicted demand for stationary and vehicle energy storage by 2040 is 4584 GWh[4]. If this growth is to be sustainable, the lifespan of deployed batteries should be as long as possible to reduce cost of replacement[5] and environmental impact. The ultimate battery should only involve a single, fully reversible charge–discharge reaction, have minimal internal resistance and retain capacity indefinitely, i.e. not degrade chemically or electrochemically. Gains in battery longevity have been made by meticulous screening to find electrodes, electrolytes and solvents[6] that decompose minimally. Yet, due to a 4.2 V potential span, electrolyte and solvent still decompose[7] to form a solid–

electrolyte interphase (SEI) on the anode[8] and a cathode–electrolyte interphase (CEI) on the cathode[9].

While the SEI is an essential yet poorly understood part of a lithium ion battery, dissolution of transition metal ions from the cathode leads to excessive SEI formation in what is known as the dissolution-migration-deposition (DMD) process, causing premature capacity fading[10] and responsible for the majority of overall capacity loss[11]. CEI however, is not typically found in aqueous rechargeable alkali batteries[12], which are greener and safer alternatives to flammable and $LiPF_6$-containing electrolyte[13]. Although these aqueous batteries also store charge reversibly, and have recently gained significant research attention for affordable energy storage[14], they also suffer from cathode dissolution mediated by acid[15] formed by fluorine-containing electrolytes in non-aqueous systems[16].

Detailed and accurate, real-time data on the dissolution of electrode materials, under all relevant operating conditions, are critical in delivering numerous scientific and technological targets: (i) to better understand the various degradation processes that occur in batteries, as a function of time, potential and charging/discharging rate; (ii) to deepen the insight in SEI and/or CEI formation, function and degradation; (iii) to propose alternative battery chemistries informed by fundamental understanding and less relying on trial and error; (iv) to inform "best practices" of battery charging and discharging to maximise lifetime; (v) to open an additional window on a battery's "state of health", diagnosing the effects of adverse events such as improper storage and charging/discharging; (vi) to quantify the impact of electrode modification, including the use of coatings, potential or other treatments, and artificial SEIs.

To date, battery electrode dissolution data are inferred by post-mortem analysis, which easily introduces errors due to multiple handling steps. More detrimentally, however, any time resolution is also lost, making the interpretation of signs of dissolution and correlation to charging/discharging history highly contrived. Recent examples include anode surface deposition mapping by laser ablation-inductively coupled plasma-mass spectrometry (LA-ICP-MS)[17] and dissolved transition metal electrolyte characterisation by total reflection X-ray fluorescence[18], where only the total lost cathode material per cycle is available. Direct observation of lithium-ion cathode dissolution has been limited to a few studies, based on rotating-ring-disk electrode (RRDE)[19], UV-vis spectrometry[20] and electron paramagnetic resonance (EPR)[21] measurements, but these methods suffer from limited selectivity and/or detection range. In an elegant recent paper, capillary electrophoresis showed remarkable ability to distinguish both element and oxidation state, and may therefore make a significant impact in upcoming battery degradation research[22].

Here, we present the first real-time dissolution study of the model cathode material $LiMn_2O_4$ (LMO) using an online flow cell–inductively coupled plasma optical emission spectrometer (ICP-OES) setup under potentiostatic and galvanostatic control. LMO dissolution has been studied previously using a post-mortem approach, leaving many important questions unanswered, including time resolution and potential dependence [23]. Online flow cell–ICP techniques, by contrast, make real-time dissolution observation possible and offer superior detection limits[24][25], but they typically use aqueous solutions unless the sample introductory system is heavily modified. Our measurements are performed with aqueous 0.2M lithium sulfate as electrolyte, mostly for compatibility reasons with the ICP torch. However, studying the dissolution of cathode materials not compounded by CEI formation—as is

generally the case in organic electrolytes—may lead to a clearer understanding of the intrinsic manganese dissolution processes.

Methods

Materials

Titanium foil (99.995%) was obtained from Advent. As electrolyte, 2.0 M Li_2SO_4 (BioUltra, Merck) was diluted with ultrapure water (MilliQ, Millipore, 18.2 MOhm cm, total organic carbon < 2 ppb) to 0.2 M; this concentration is lower than in typical lab batteries (2 M), but its impact on achievable capacity and iR drop in aqueous solutions has been reported as minimal [26]. $LiMn_2O_4$ (LMO) powder (Mesh-325), dimethylsulfoxide (DMSO, ACS grade), Super-P carbon and polyvinylidene difluoride (PVDF) powder were obtained from Alfa Aesar.

$LiMn_2O_4$ electrode preparation

LMO powder, Super-P carbon and PVDF were added to DMSO (2 mL) in a 20:6:1 mass ratio for a total solids mass of 27 mg. DMSO is much safer than N-methylpyrrolidone and has been recently shown to be a promising green alternative with comparable slurry properties[27]. To disperse the solids, the mixture was magnetically stirred for 24 hours, sonicated for 30 minutes, and shaken vigorously. A cut-out piece of titanium foil was polished successively with 1.0, 0.3 and 0.05 μm homogenised alumina suspension (Buehler) and thoroughly rinsed with MilliQ water, before drying by N_2 blasting. To achieve a loading of 100 μg cm^{-2}, for a geometric electrode area of 0.636 cm^2, 6 μL of the suspension was deposited onto the titanium foil using an air displacement pipette. The titanium current collector was chosen due to its low activity towards the oxygen evolution reaction (OER) [28] which may take place on stainless steel at high states of charge and cause electrochemical interference. Unlike stainless-steel alloys, Ti also does not contain manganese which may interfere with ICP-OES analysis by

introducing artefacts. In view of the high boiling point of DMSO, the deposited ink was heated by an infrared lamp to accelerate the evaporation of the solvent. Higher ink loadings were avoided as these frequently led to mechanical cracking and detachment of the dried ink from the current collector.

Online electrochemical flow cell–ICP-OES

A lab-built, two-compartment droplet flow cell was used for online ICP-OES measurements, **Figures 1** and **2**. Similar to the flow through scanning droplet cell described by Schuppert et al.[29] the droplet through which the electrolyte solution flows is exposed at the bottom so that a solid sample can be raised up and closes the electrochemical circuit upon wetting. An ethylene propylene diene monomer (EPDM) rubber O-ring was glued to the edge of the opening using two-component epoxy glue (RS-components), defining a 0.636 cm^2 working electrode area. A flow rate of 1.5 mL min^{-1} was used to transport dissolution products away from the working electrode, using the onboard ICP-OES peristaltic pump downstream of the cell. As with the atomic emission spectroelectrochemical cell described by Ogle et al.[30], the stagnant electrolyte compartment contained a 15 cm^2 carbon cloth counter electrode (Panex PW06, Zoltech) and was separated from the flow compartment by a microporous polypropylene separator membrane (Celgard 3401). The reference electrode (RE) was a Leak-Free (LF-1) Ag/AgCl/3.4 M. KCl electrode (Innovative Instruments) positioned upstream of the working electrode compartment; all potential values in this paper are with reference to this RE.
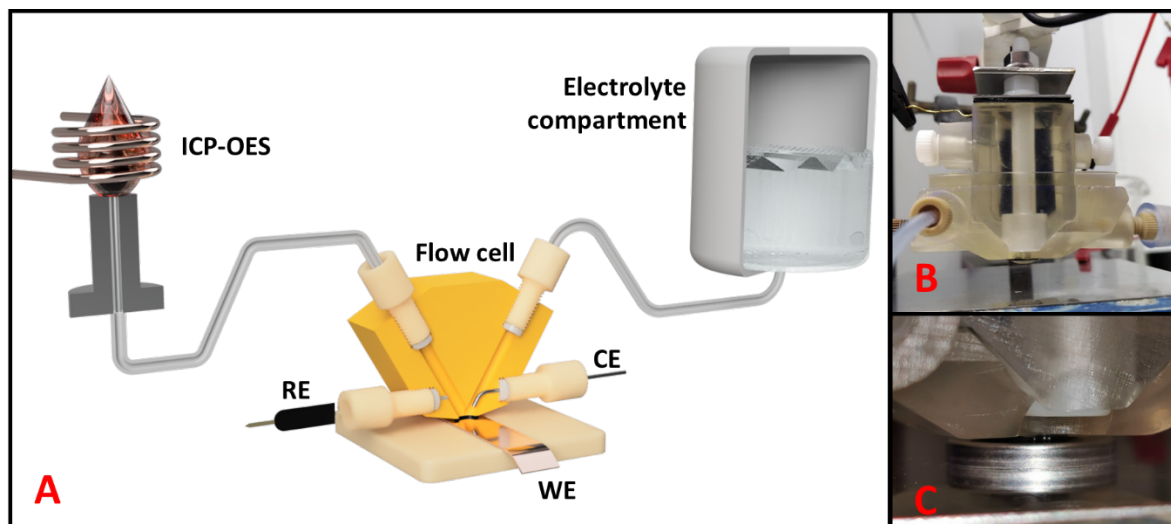
Figure 1. A) Cross-section diagram of the online flow cell ICP-OES setup. B) Photograph of the in-house built two-compartment droplet flow cell. C) The flow cell in contact mode with a compressed exposure O-ring.
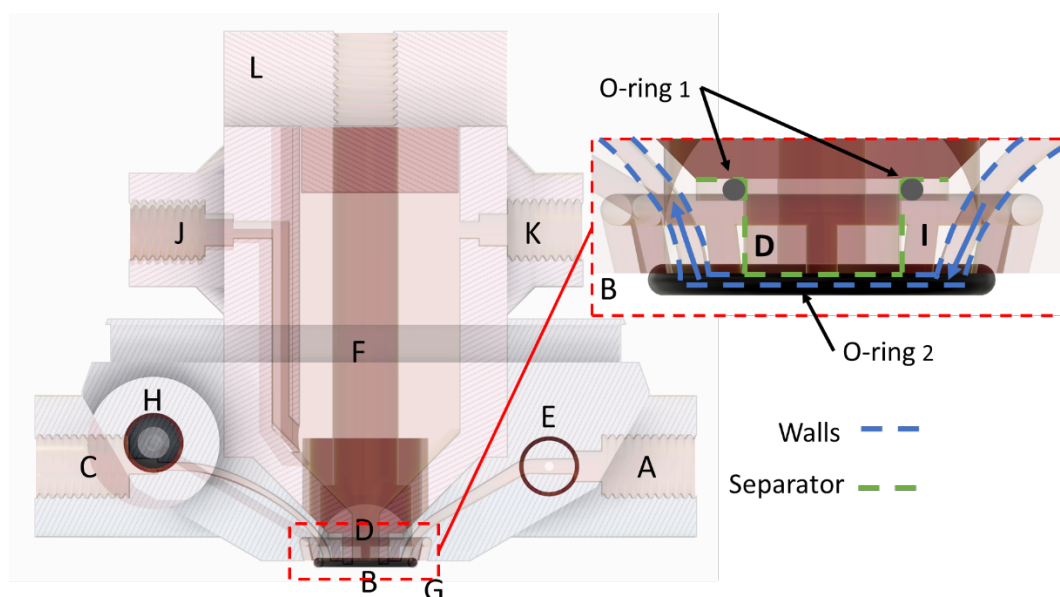

Figure 2. Cross-section scheme of the two-compartment flow cell. A) electrolyte inlet B) flow compartment C) electrolyte outlet D) separator E) reference electrode port F) stagnant counter electrode compartment G) working electrode sealing O-ring H) nitrogen inlet port I) nitrogen shield channels.

The ICP-OES was an Agilent 5100 dual-view instrument fitted with a Seaspray nebuliser, double-pass cyclonic spray chamber and 2.8 mm wide bore torch for high total dissolved solids applications. Due to a manufacturer recommended upper limit of 20 g L^{-1} total dissolved solids, the concentration of Li_2SO_4 was limited to 0.2 M. Data was acquired through the ICP Expert software LiveView feature, and the timestamps of the ICP-OES and the BioLogic SP-200 potentiostat/galvanostat were synchronised by comparing 12 one-minute long dissolution pulse intervals of zinc anodisation steps while monitoring the zinc emission signal at 213.856 nm. Manganese was monitored at 257.610 nm emission wavelength. Standard solutions between zero (blank) and 1 ppm were prepared by diluting 5, 10, 20, 30, 40 and 50 μL of 1000 ppm manganese ICP standard (Sigma–Aldrich) to 50 mL using 0.2 M Li_2SO_4; taking into account the cell footprint and electrolyte flow rate, these standard solutions cover an instantaneous Mn dissolution range between zero and 39 ng s^{-1} cm^{-2}. A limit of detection (LOD) between 0.015 ng s^{-1} cm^{-2} and 0.016 ng s^{-1} cm^{-2} was estimated for Mn by multiplying the standard deviation of a blank solution across 10 measurements by 3[31]. Assuming a standard normal distribution, the probability of a false positive signal 0.015 ng s^{-1} cm^{-2} from the mean blank signal is $(1-0.9987) \times 100 = 0.13\%$. We subtract the mean blank signal from the spectroscopic data instead of adding it to the calculated detection limit.

The manganese standards yielded a linear relationship in the trace concentration range 0.1 - 1.0 ppm for the 257.610 nm wavelength. Spectroscopic intensity was converted to dissolution rate using

$$m_{Mn} = \frac{m_f \times f \times 10^6 \ ng \ mg^{-1}}{A}$$

where m_{Mn} is the dissolution rate in ng s^{-1} cm^{-2}, m_f the instantaneous dissolution concentration in mg kg^{-1}, f the flow rate in kg s^{-1} and A the electrode area in cm^2. The geometric area was that of the area defined by the flow cell O-ring, as the LMO particle size uncertainty (mesh-325) was large.

Results

Figure 3 shows cyclic voltammograms of a freshly prepared LMO electrode and the concurrent manganese dissolution rate, starting at the open circuit potential (OCP) after stabilisation for 30 minutes. Already during the first anodic scan, from OCP to 0.45 V, manganese dissolution is detected and increases to a maximum at 0.20 V, before falling below the detection limit, even as the potential scan direction is reversed.

During subsequent scans, with gradually increasing positive vertex potential (**Figure 3**, panels B-E), no further Mn dissolution is detected as long as the potential remains below +1.2V. The anodic lithium extraction and cathodic insertion peaks agree well with published voltammograms in the same electrolyte [32]. In the range from 0.3 to 1.1 V, no dissolution features were observed above the detection limit that correlate to the order/disorder transition peaks of LMO, contrary to RRDE studies conducted in aprotic LiPF6 electrolyte[33], where Mn dissolution was found to increase rapidly at 90-100% state of charge (SoC). On our potential scale, this would correspond to 0.75-1.0 V, and no Mn is detected; only in the fifth scan (panel E), Mn dissolution is again detected for potentials above 1.2 V, well beyond 100% SoC and seemingly in the oxygen evolution region. In aprotic, LiPF$_6$ / carbonate systems dissolution of manganese at 90-100% SoC may be promoted by carbonate oxidation and subsequent HF formation which may attack the LMO surface[34].
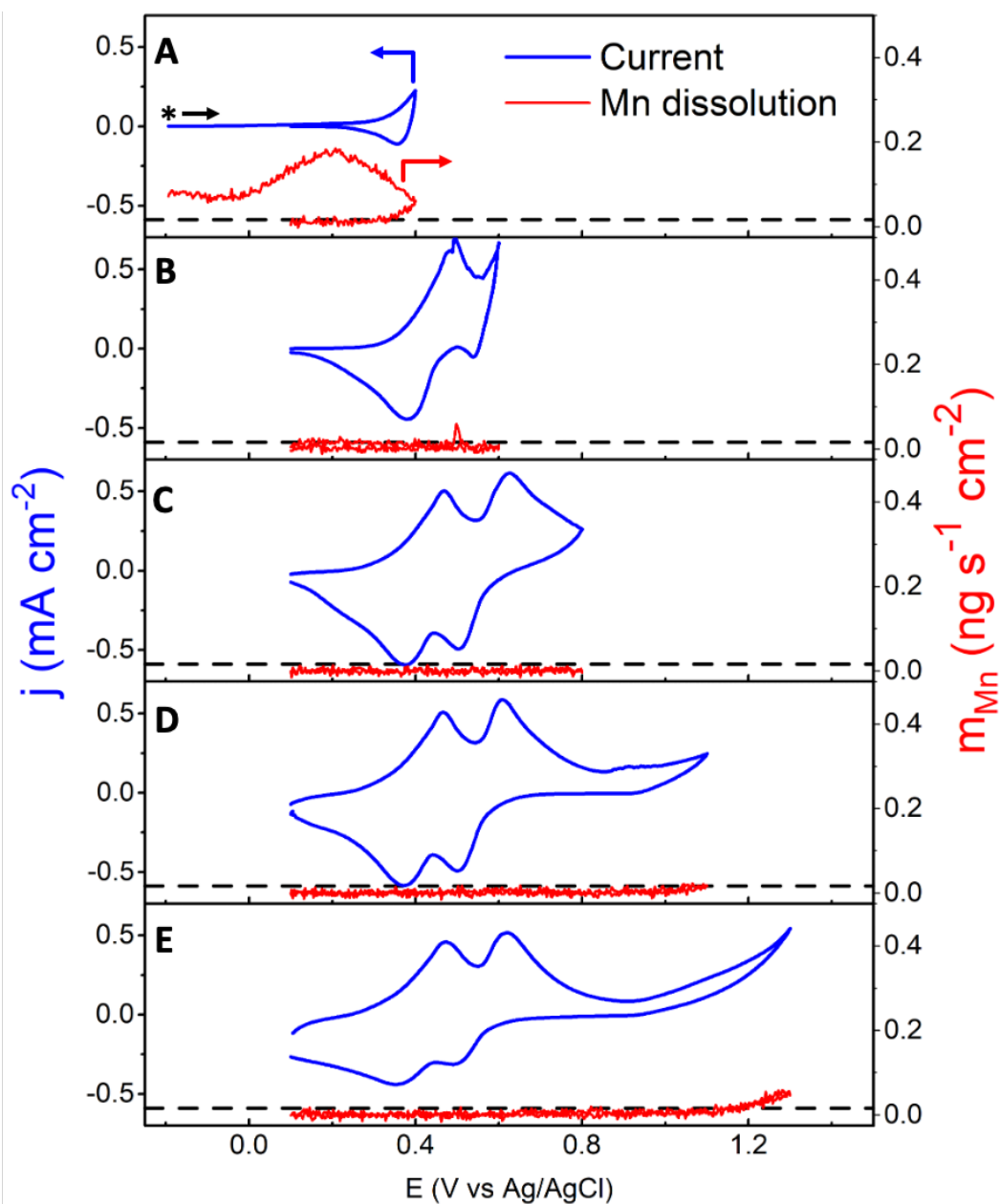
Figure 3. Cyclic voltammograms (blue traces, left axis) and simultaneous Mn dissolution rates (red traces, right axis) of dropcast LMO in 0.2 M Li_2SO_4 with increasingly positive vertex potential (panels A-E). The starting potential is indicated with an asterisk. Scan rate 2 mV s^{-1}, flow rate 1.5 mL min^{-1}. The dashed line represents the 3σ detection limit of manganese.

To investigate this behaviour in more detail, **Figure 4** shows four consecutive cyclic voltammograms, preceded by a 30-minute OCP period following initial contact with the LMO electrode. Immediately after wetting of the LMO by the electrolyte, which itself may depend

on the microscopic details of the electrode surface [55], the manganese dissolution rate reaches 0.35 ng s^{-1} cm^{-2}, before decreasing exponentially to 0.1 ng s^{-1} cm^{-2} after 30 minutes. Over the same period, the electrode OCP value rises from –0.30 V to –0.20 V. Based on the Pourbaix diagram of manganese, this potential value suggests that Mn(II) is present [35]. The presence of sulfate anions increases the solubility of Mn(OH)$_2$ precipitates[36], which may explain that any lower valence manganese oxide or hydroxide on the surface of the LMO particles is dissolved by the initial contact of Li$_2$SO$_4$ solution on electrode wetting.
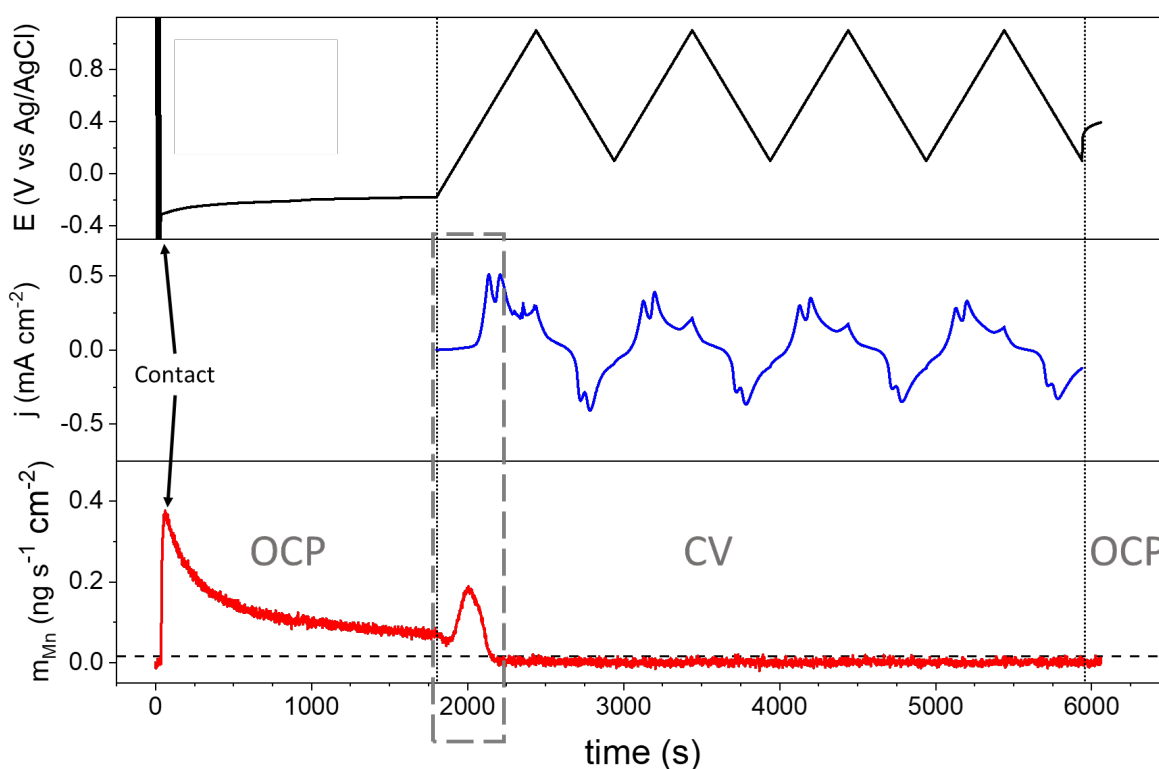

Figure 4. Potential (top), current (middle) and Mn dissolution rate (bottom panel) as a function of time after contacting a dropcast LMO electrode with 0.2M Li$_2$SO$_4$ at time zero. OCP and CV (4 cycles, scan rate 2mV s^{-1}) regions as indicated. Flow rate, 1.5 mL min^{-1}. The dashed line represents the 3σ detection limit of Mn.

During the first anodic scan, starting at 1800 s, the manganese dissolution rate passes through a maximum of 0.2 ng s^{-1} cm^{-2}, before falling below the detection limit for the rest of the experiment. After the four cycles, the OCP approaches 0.4V, 0.6V more positive than before

cycling and indicating that the LMO electrode was not returned to its initial state. In the entire experiment, no Mn was detected in the electrolyte after the initial anodic scan, starting at t=1800s. The maximum in dissolution rate, at t = 2000s, is accompanied by a slight shoulder in the current trace, in the potential region between 0 and 0.3V. In sulfate electrolyte, oxidation features in this region have been linked to conversion of Mn_3O_4 to Mn_2O_3[37], which would correspond to a change in the average Mn oxidation state from 2.67 to 3.

The dissolution–passivation feature at 2000s appears to be of particular significance, as it separates regions of active Mn dissolution before the maximum from undetectable Mn levels in the electrolyte after. In order to analyse this feature (highlighted by a dashed box in **Figure 4**) in more detail, we show a magnification in **Figure 5**. By fitting an exponentially increasing baseline to the initial and final segments of the current trace, we can integrate the charge corresponding to the shoulder in the voltammogram, yielding 1.41 mC cm^{-2}. For the sake of comparison, we also convert the Mn dissolution signal into an equivalent current, assuming a 1-electron Faraday process and considering that

$$j_{Mn} = \frac{m_{Mn} z F}{M_{Mn}}$$

where M_{Mn} = 54.938 × 10^9 ng mol^{-1} is the relative atomic mass of manganese, F = 96485 C mol^{-1} Faraday's constant and z = 1 the assumed charge transfer number for the dissolution process. The conversion thus assumes that each manganese ion detected by ICP-OES contributes one electron to the equivalent manganese dissolution current j_{Mn}, which is plotted in **Figure 5**. Integrating the peak in j_{Mn} yields 59.0 μC cm^{-2} (equivalent to Mn dissolution of 33 ng cm^{-2}), which is less than 5% of the electrochemical charge producing the shoulder in the voltammogram. Clearly, therefore, the current shoulder cannot be explained by a 1-electron

anodic dissolution process, but may instead be related to electrochemical oxidation of the surface itself, mostly without forming soluble Mn products [38]:

$$j_{ext} = j_{diss} + j_{film} + \ldots$$

where the total current (j_{total}) consists of direct anodic dissolution (j_{diss}) and other contributions (e.g. film formation, j_{film}).

So far, we have established that Mn dissolution occurs when a pristine LMO electrode is exposed to sulfate electrolyte under open circuit conditions, but that this dissolution ceases as soon as a single anodic scan over 0.5V has occurred.
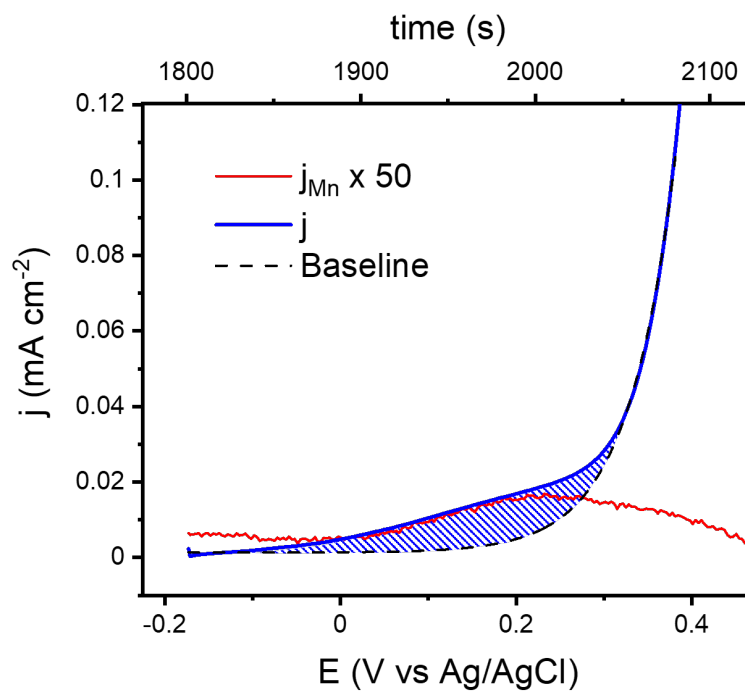

Figure 5. Magnified initial anodic scan (from Figure 4), revealing a shoulder in the current trace. The concurrent Mn dissolution signal has been converted to an equivalent current, assuming a 1-electron Faraday process.

To investigate the behaviour under conditions of overlithiation or, in battery science terminology, overdischarge, a fresh LMO electrode was first passivated by brief anodic

13

polarisation, **Figure 6A**, before going to more negative potentials, **Figure 6B**. As the potential passes – 0.1 V, a nonzero cathodic current is accompanied by reactivation of manganese dissolution, increasing exponentially before tailing off at – 0.7 V. During the return scan, the instantaneous Mn dissolution remains significant, with peaks at – 0.2 V and + 0.2 V, and only falls below the detection limit when the potential is increased above 0.5 V, similar as in **Figures 3** and **4**; this behaviour was consistent during subsequent cycles. We note that the Mn dissolution in the overlithiation region is an order of magnitude more intense than in the delithiation region discussed earlier. This is most striking in **Figure 6A**, where the dissolution–passivation feature is almost invisible on the vertical scale that is relevant for **Figure 6B**, and may be a further indication that the anodic behaviour is limited to the surface, while the cathodic behaviour involves the bulk of the electrode. The dissolution peaks correspond to 1.8 μA cm^{-2} at -0.18 V and 1.6 μA cm^{-2} at 0.15V, almost an order of magnitude lower than electrochemical features at 7.4 μA cm^{-2} and 14 μA cm^{-2} respectively.
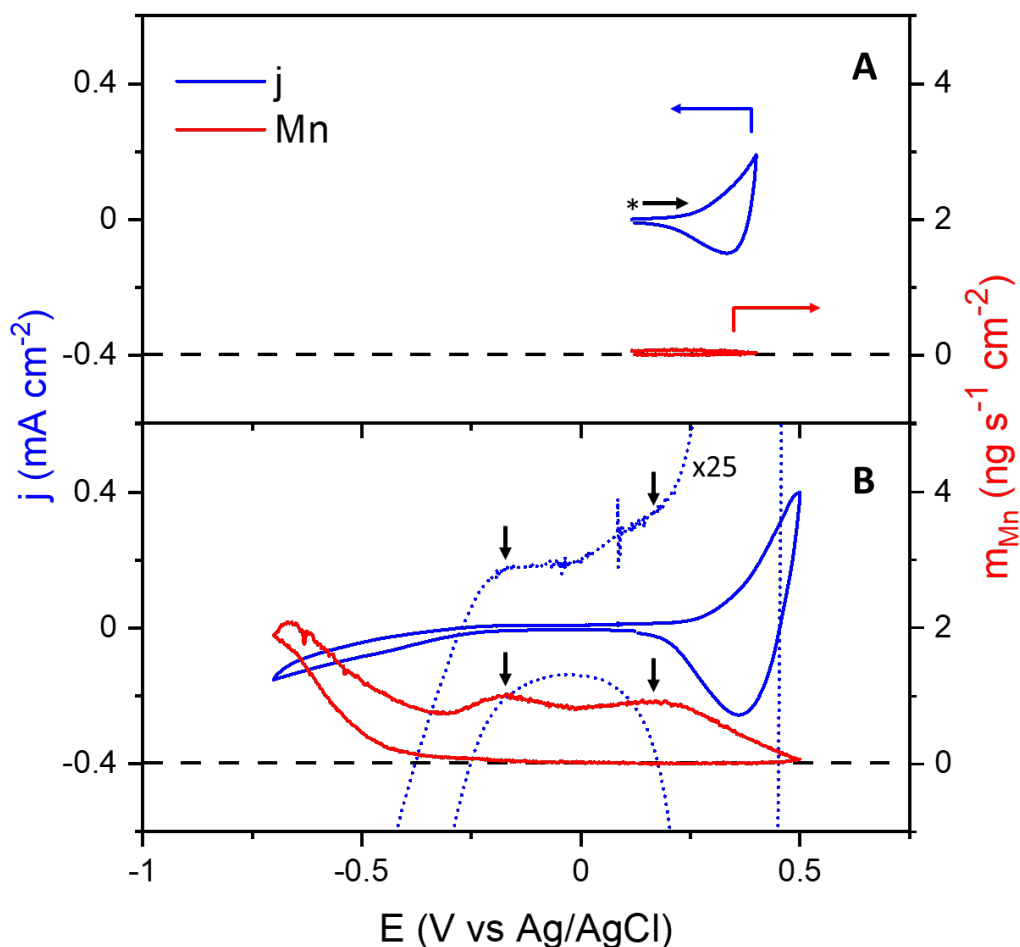
Figure 6. Cyclic voltammograms (blue traces, left axis) and instantaneous Mn dissolution rates (red traces, right axis) of dropcast LMO in 0.2 M Li_2SO_4, exploring the negative potential region where overlithiation takes place (panel B), after brief anodic potential excursion to passivate the surface (panel A). The starting potential is indicated with an asterisk. Scan rate 2 mV s^{-1}, 1.5 mL min^{-1} flow rate.

The Mn dissolution patterns discussed above were also confirmed using a galvanostatic charging–discharging protocol, **Figure 7**. Measuring in the same potential range by galvanostatic programming reveals the same dissolution pattern as observed in cyclic voltammetry, including manganese dissolution after initial delithiation. When the LMO electrode is switched from OCP to galvanostatic charging after 1600 s, a sharp dissolution peak accompanies the electrode potential rising from – 0.1 V to 0.4 V, before decaying below the detection limit. Integration of the peak yields a total mass loss of manganese during this event of 21.6 ng cm^{-2}.
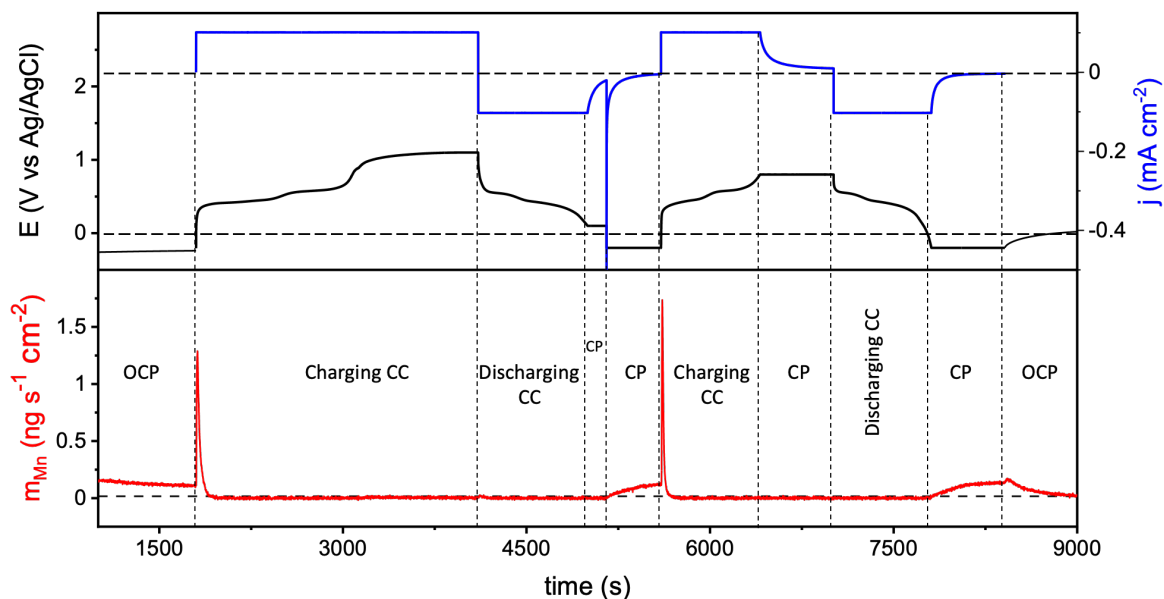
Figure 7. Galvanostatic charging–discharging of dropcast LMO electrode (top) and instantaneous Mn dissolution rate (bottom) in 0.2 M Li_2SO_4. OCP, constant current (CC) and constant potential (CP) regions as indicated.

After the two phase transition potential plateaus from delithiation[39], a third plateau at 1.1 V appears at 3000 s, which may correspond to oxygen evolution on the LMO electrode[40], however without detectable Mn dissolution. At this point, galvanostatic discharging was started using the same but opposite current density, until a potential of 0.1 V was reached at 4900 s; this end-of-discharge potential was held for 300s to allow the electrode to homogenise at the knee-point. To investigate under which conditions Mn dissolution rekindles, the potential was stepped down at 5200s to – 0.1 V, the OCP value just before initial charging. Immediately, the Mn dissolution resumes, and over time again approaches 0.1 ng s^{-1} cm^{-2}, while the cathodic current density for lithium insertion approaches zero. The dissolution rate at 0% SoC is therefore consistent, and not dependent on whether the corresponding potential is assumed spontaneously (as true OCP) or is imposed.

A second charging cycle starts at 5600 s, again with an initial spike in manganese dissolution rate to above 1 ng s^{-1} cm^{-2}, shortly followed by passivation. The total manganese mass loss during the spike at 5600 s is 27.8 ng cm^{-2}, close to the mass loss determined from the first dissolution peak at 1600 s and from the cyclic voltammogram in Figure 2. A potentiostatic segment (6500–7000s, at 100% charge) does not cause dissolution. Only a return to – 0.1 V, at the end of discharge at 7800 s, restarts manganese dissolution. When potential control is released at 8100 s, the OCP increases towards 0 V while Mn dissolution tails off, suggesting that the LMO electrode was not fully lithiated before being relaxed, and therefore immune to dissolution.

Discussion

Central in the understanding of Mn dissolution from its oxides is its oxidation state, and our data in delithiated and overlithiated regimes show this effect immediately. In LMO (LiMn^{III}Mn^{IV}O$_4$) at full lithiation, the average Mn oxidation state is 3.5, and Mn dissolution from this material is typically explained by invoking Hunter's mechanism of acid-mediated disproportiation [41]:

$$2LiMn_2O_4 + 4H^+ \rightarrow 3\lambda MnO_2 + Mn^{2+} + 2Li^+ + 2H_2O$$
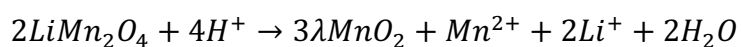
where Mn(III) forms highly soluble Mn(II) and insoluble Mn(IV) species. As the electrode potential increases and delithiation starts, the equation predicts a decreasing rate of dissolution, proportional with the increasingly sparse Mn(III) sites at the surface. Our data, however, both potentiostatic and galvanostatic, show a marked increase in dissolution rate upon initial charging, immediately followed by Mn dissolution becoming undetectable, very much like a classic anodic dissolution–passivation transition during metal passivation. This

observation alone indicates that Hunter's mechanism in isolation cannot explain the observed behaviour. Furthermore, Hunter's mechanism is acid-driven, and DFT calculations have shown that this pathway becomes energetically unfavourable above pH 4-5, such as in the electrolyte we use[42]. The dramatic increase in Mn dissolution during initial delithiation of LMO, followed by an even more abrupt end to the dissolution as the potential is made more positive, may indicate a dissolution–precipitation mechanism, or a compositional or phase change of the electrode surface layer, the nature of which is as yet unclear. A detailed understanding of these surface changes will require in-depth surface analyses.

In studies on $LiPF_6$-containing LMO batteries, post-mortem elemental analysis of the lithium anode suggested that the greatest Mn dissolution took place for batteries stored below 30% SoC and above 90% SoC, with a middle region (30% to 80% SoC) where manganese dissolution was low but not zero, and that smaller LMO particle sizes yielded more dissolution[43]. Some of the discrepancy between manganese dissolution in aqueous and non-aqueous electrolytes may be explained by Mn(II) and Mn(III) stability in aqueous Li_2SO_4 and non-aqueous $LiPF_6$ electrolyte, as Mn(III)-containing dissolution products have been identified in non-aqueous electrolyte by EPR[44], and Mn(III) dissociation pathways in presence of F^- may be possible[45].

In the present study, we did not observe Mn dissolution within the (de)intercalation window itself, or even 0.4 V beyond the second phase transition peak of lithium deintercalation, as opposed to Wang et al.[33] and Zhao et al. [20]. However, in most dissolution experiments[46][47][19][20], or indeed in standard lithium-ion coin cells, stainless steel is used as a current collector, where manganese can constitute up to 10% of the mass depending

on the alloy. Some manganese detected in the electrolyte may therefore be a current-collector-induced artefact and not originate from the active electrode material.

Mn dissolution was again detected at very positive potentials, past full deintercalation of Li^+ from the λ-MnO$_2$ host structure. In LiPF$_6$–carbonate electrolytes, the delithiated λ-MnO$_2$ surface is found to be unstable and breaks down to Mn$_3$O$_4$ (Mn^{II}Mn$^{III}_2$O$_4$) which contains a higher proportion of Mn(III) and also free Mn(II), both of which could lead to more dissolution [48][49]. This degradation, however, was found at a less positive potential (4.3 V vs Li^+/Li) compared to our findings and may not explain our observation. Another phase transition to O3-layered MnO$_x$ structure or O^{2-} redox at 5.1 V vs Li^+/Li which corresponds to significant overcharging has also been identified[50]. This potential range corresponds better to the dissolution rates observed in Figure 1, about 1 V positive of the first phase transition peak in the voltammograms, suggesting that we reached the onset of this phase transition at 1.2 V vs Ag/AgCl, with concurrent oxygen evolution from the electrode. In both cases, these surface species disappear after discharge, possibly due to dissolution. Although Mn dissolution from the degradation process at 4.3 V vs Li^+/Li was not observed here, this could be due to an insufficient detection limit of the ICP-OES setup. Moving forward, it may be possible to isolate and study in more detail individual Mn dissolution processes by tuning electrolyte and solvent.

Overlithiation (at potentials negative from the initial OCP) produces very different while active Mn dissolution behaviour, in line with RRDE collection experiments [46] and increased capacity fade and dissolution due to the lower average Mn oxidation state in Li$_2$Mn$^{III}_2$O$_4$[51], promoting Mn(III) disproportiation. For these overlithiated structures, DFT calculations found Hunter's mechanism to remain energetically favourable up to pH 8 [42],

which may explain the increased dissolution rate upon cathodic polarisation we observe. In non-aqueous electrolytes, spiking the electrolyte with Mn^{2+} causes a decrease in reductive peak intensity, another argument in support of this interpretation[52]. Tetragonal $Li_2Mn_2O_4$ therefore appears consistently more unstable compared to $LiMn_2O_4$.

While our measurements confirm the instability of fully lithiated and especially overlithiated LMO electrodes, the large discrepancies between reported Mn dissolution in aprotic electrolytes and the current work also show that electrolyte nature and composition have a major impact on battery electrode stability. Furthermore, careful design of charging/discharging profiles to avoid the electrode from entering potential regions characterised by intense Mn dissolution, may be a viable alternative to the use of surface coatings or artificial CEIs[15] in optimising battery life.

Our data reveal very detailed dissolution information, and also suggest whether dissolution events or regions are related to a surface state or process, such as superficial oxidation, or to bulk properties of the electrode under study, such as structural strain from Li^+ intercalation, which constitutes the majority of the measured current. In the battery field, the vast majority of efforts is aimed at increasing performance through careful optimisation of bulk synthesis, with extensive characterisation of crystallography, etc. Every electrode material, however, interacts with its environment through its surface, so that the details and properties of the latter are of overwhelming importance, including those of the double layer after the electrode–electrolyte interface has been established, and possible additional phases have formed (SEI, CEI). For fundamental energy minimising reasons, the structure of a solid surface necessarily differs from that of the bulk, sometimes leading to striking surface reconstructions, affecting its reactivity, even in the absence of dangling bonds. For this reason, the importance of

experimental and theoretical surface science investigations of battery electrode materials can hardly be overestimated.

Conclusion and outlook

By coupling a flow-through electrochemical cell to an ICP-OES, we have obtained detailed Mn dissolution data from a dropcast $LiMnO_2$ (LMO) electrode in aqueous 0.2 M Li_2SO_4, as a function of both time and potential/state of charge. Fully lithiated LMO, with an average Mn redox state of 3.5, readily dissolves when contacted by 0.2M Li_2SO_4, but initial charging that precedes delithiation abruptly stops further detectable dissolution, until well past fully delithiated λ-MnO_2. In marked contrast with aprotic electrolytes, we found no correlation between dissolution and the lithium insertion-extraction process. Dissolution resumes on returning to the initial potential of pristine LMO, and increases exponentially in the overlithiation region. Our results provide access to much more detailed dissolution information than post-mortem battery analysis allows, enabling targeted materials screening and informing best practices in charging/discharging profiles. In particular, our data suggests that suitable potential conditioning of electrodes may mitigate dissolution, as an alternative or additional measure to the use of protective surface films or incorporation of dopants.

As an outlook, the very detailed, real-time dissolution information to which our method gives access allows to investigate in a straightforward manner the effect of many variables: electrode material particle size, presence of dopants, film thickness (differentiating between "thin film" or "thick film" regimes, depending on whether the entire film participates in the behaviour or only superficially[53]). Demonstrated here for a dropcast electrode, the in situ flow-through droplet cell allows investigation of commercial electrodes and materials with

minimal modifications, but also single crystals and thin films produced using pulsed laser deposition methods [54], which make in-depth surface characterisation easier.

References

[1]   B. Scrosati, History of lithium batteries, J. Solid State Electrochem. (2011). https://doi.org/10.1007/s10008-011-1386-8.

[2]   N. Armaroli, V. Balzani, Towards an electricity-powered world, Energy Environ. Sci. 4 (2011) 3193. https://doi.org/10.1039/c1ee01249e.

[3]   IEA, Key World Energy Statistics 2020, 2020. https://www.iea.org/reports/key-world-energy-statistics-2020.

[4]   BloombergNEF, Energy Storage Outlook 2019, 2019. https://about.bnef.com/blog/energy-storage-investments-boom-battery-costs-halve-next-decade/.

[5]   D. Larcher, J.M. Tarascon, Towards greener and more sustainable batteries for electrical energy storage, Nat. Chem. (2015). https://doi.org/10.1038/nchem.2085.

[6]   J.B. Goodenough, Y. Kim, Challenges for rechargeable Li batteries, Chem. Mater. (2010). https://doi.org/10.1021/cm901452z.

[7]   A. Guéguen, D. Streich, M. He, M. Mendez, F.F. Chesneau, P. Novák, E.J. Berg, Decomposition of LiPF 6 in High Energy Lithium-Ion Batteries Studied with Online

Electrochemical Mass Spectrometry , J. Electrochem. Soc. (2016). https://doi.org/10.1149/2.0981606jes.

[8] Y. Dai, L. Cai, R.E. White, Capacity Fade Model for Spinel LiMn 2 O 4 Electrode , J. Electrochem. Soc. 160 (2013) A182–A190. https://doi.org/10.1149/2.026302jes.

[9] X.T. Wang, Z.Y. Gu, W.H. Li, X.X. Zhao, J.Z. Guo, K. Di Du, X.X. Luo, X.L. Wu, Regulation of Cathode-Electrolyte Interphase via Electrolyte Additives in Lithium Ion Batteries, Chem. - An Asian J. (2020). https://doi.org/10.1002/asia.202000522.

[10] Y.K. Lee, J. Park, W. Lu, A Comprehensive Study of Manganese Deposition and Side Reactions in Li-Ion Battery Electrodes, J. Electrochem. Soc. (2017). https://doi.org/10.1149/2.1851712jes.

[11] C. Zhan, J. Lu, A. Jeremy Kropf, T. Wu, A.N. Jansen, Y.K. Sun, X. Qiu, K. Amine, Mn(II) deposition on anodes and its effects on capacity fade in spinel lithium manganate-carbon systems, Nat. Commun. (2013). https://doi.org/10.1038/ncomms3437.

[12] F. Wang, Y. Lin, L. Suo, X. Fan, T. Gao, C. Yang, F. Han, Y. Qi, K. Xu, C. Wang, Stabilizing high voltage LiCoO2 cathode in aqueous electrolyte with interphase-forming additive, Energy Environ. Sci. (2016). https://doi.org/10.1039/c6ee02604d.

[13] W. Li, J.R. Dahn, D.S. Wainwright, Rechargeable Lithium Batteries with Aqueous Electrolytes, Science (80-.). 264 (1994) 1115–1118.

[14] H. Kim, J. Hong, K.Y. Park, H. Kim, S.W. Kim, K. Kang, Aqueous rechargeable Li and Na ion batteries, Chem. Rev. 114 (2014) 11788–11827. https://doi.org/10.1021/cr500232y.

[15] J. Zhi, K. Bertens, A.Z. Yazdi, P. Chen, Acrylonitrile copolymer/graphene skinned cathode for long cycle life rechargeable hybrid aqueous batteries at high-temperature, Electrochim. Acta. 268 (2018) 248–255.

https://doi.org/10.1016/j.electacta.2018.02.098.

[16]   M. Stich, M. Göttlinger, M. Kurniawan, U. Schmidt, A. Bund, Hydrolysis of LiPF6 in

Carbonate-Based Electrolytes for Lithium-Ion Batteries and in Aqueous Media, J.

Phys. Chem. C. 122 (2018) 8836–8842. https://doi.org/10.1021/acs.jpcc.8b02080.

[17]   T. Schwieters, M. Evertz, A. Fengler, M. Börner, T. Dagger, Y. Stenzel, P. Harte, M.

Winter, S. Nowak, Visualizing elemental deposition patterns on carbonaceous anodes

from lithium ion batteries: A laser ablation-inductively coupled plasma-mass

spectrometry study on factors influencing the deposition of lithium, nickel, manganese

and cobalt after dissolution, J. Power Sources. 380 (2018) 194–201.

https://doi.org/10.1016/j.jpowsour.2018.01.088.

[18]   M. Evertz, J. Kasnatscheew, M. Winter, S. Nowak, Investigation of various layered

lithium ion battery cathode materials by plasma- and X-ray-based element analytical

techniques, Anal. Bioanal. Chem. 411 (2019) 277–285. https://doi.org/10.1007/s00216-

018-1441-8.

[19]   J.S. Chen, L.F. Wang, B.J. Fang, S.Y. Lee, R.Z. Guo, Rotating ring-disk electrode

measurements on Mn dissolution and capacity losses of spinel electrodes in various

organic electrolytes, J. Power Sources. 157 (2006) 515–521.

https://doi.org/10.1016/j.jpowsour.2005.08.019.

[20]   L. Zhao, E. Chénard, Ö.Ö. Çapraz, N.R. Sottos, S.R. White, Direct Detection of

Manganese Ions in Organic Electrolyte by UV-vis Spectroscopy, J. Electrochem. Soc.

165 (2018) A345–A348. https://doi.org/10.1149/2.1111802jes.

[21]   A. Banerjee, Y. Shilina, B. Ziv, J.M. Ziegelbauer, S. Luski, D. Aurbach, I.C. Halalay,

On the oxidation state of manganese ions in li-ion battery electrolyte solutions, J. Am.

Chem. Soc. 139 (2017) 1738–1741. https://doi.org/10.1021/jacs.6b10781.

[22]   L. Hanf, J. Henschel, M. Diehl, M. Winter, S. Nowak, Mn2+ or Mn3+? Investigating

transition metal dissolution of manganese species in lithium ion battery electrolytes by capillary electrophoresis, Electrophoresis. 41 (2020) 697–704. https://doi.org/10.1002/elps.201900443.

[23]   A. Bhandari, J. Bhattacharya, Review—Manganese Dissolution from Spinel Cathode: Few Unanswered Questions, J. Electrochem. Soc. 164 (2017) A106–A127. https://doi.org/10.1149/2.0101614jes.

[24]   K. Ogle, S. Weber, Anodic Dissolution of 304 Stainless Steel Using Atomic Emission Spectroelectrochemistry, J. Electrochem. Soc. 147 (2000) 1770. https://doi.org/10.1149/1.1393433.

[25]   S.O. Klemm, A. Karschin, A.K. Schuppert, A.A. Topalov, A.M. Mingers, I. Katsounaros, K.J.J. Mayrhofer, Time and potential resolved dissolution analysis of rhodium using a microelectrochemical flow cell coupled to an ICP-MS, J. Electroanal. Chem. 677–680 (2012) 50–55. https://doi.org/10.1016/j.jelechem.2012.05.006.

[26]   N. Alias, A.A. Mohamad, Advances of aqueous rechargeable lithium-ion battery: A review, J. Power Sources. 274 (2015) 237–251. https://doi.org/10.1016/j.jpowsour.2014.10.009.

[27]   M. Wang, X. Dong, I.C. Escobar, Y.T. Cheng, Lithium Ion Battery Electrodes Made Using Dimethyl Sulfoxide (DMSO) - A Green Solvent, ACS Sustain. Chem. Eng. (2020). https://doi.org/10.1021/acssuschemeng.0c02884.

[28]   E.M. Oliveira, C.E.B. Marino, S.R. Biaggio, R.C. Rocha-Filho, Reactivation of passive titanium: The enhancement of O2 evolution after potentiodynamic cyclings, Electrochem. Commun. 2 (2000) 254–258. https://doi.org/10.1016/S1388-2481(00)00018-7.

[29]   A.K. Schuppert, A.A. Topalov, I. Katsounaros, S.O. Klemm, K.J.J. Mayrhofer, A Scanning Flow Cell System for Fully Automated Screening of Electrocatalyst

Materials, J. Electrochem. Soc. (2012). https://doi.org/10.1149/2.009211jes.

[30] V. Shkirskiy, P. Maciel, J. Deconinck, K. Ogle, On the time resolution of the atomic

emission spectroelectrochemistry method, J. Electrochem. Soc. 163 (2016) 1–8.

https://doi.org/10.1149/2.0991602jes.

[31] A. Shrivastava, V. Gupta, Methods for the determination of limit of detection and limit

of quantitation of the analytical methods, Chronicles Young Sci. (2011).

https://doi.org/10.4103/2229-5186.79345.

[32] A. Tron, Y.D. Park, J. Mun, AlF3-coated LiMn2O4 as cathode material for aqueous

rechargeable lithium battery with improved cycling stability, J. Power Sources. 325

(2016) 360–364. https://doi.org/10.1016/j.jpowsour.2016.06.049.

[33] L.F. Wang, C.C. Ou, K.A. Striebel, J.S. Chen, Study of Mn dissolution from LiMn2O4

spinel electrodes using rotating ring-disk collection experiments, J. Electrochem. Soc.

(2003). https://doi.org/10.1149/1.1577543.

[34] A. Guéguen, D. Streich, M. He, M. Mendez, F.F. Chesneau, P. Novák, E.J. Berg,

Decomposition of LiPF 6 in High Energy Lithium-Ion Batteries Studied with Online

Electrochemical Mass Spectrometry , J. Electrochem. Soc. 163 (2016) A1095–A1100.

https://doi.org/10.1149/2.0981606jes.

[35] J. Hem, Chemical equilibria and rates of manganese oxidation - Chemistry of

Manganese in Natural Water, US Geol. Surv. Water-Supply Pap. 1667-A. (1963) 71.

https://pubs.usgs.gov/wsp/1667a/report.pdf.

[36] J.D. Hem, Manganese Complexes with Bicarbonate and Sulfate in Natural Water, J.

Chem. Eng. Data. 8 (1963) 99–101. https://doi.org/10.1021/je60016a029.

[37] J.N. Broughton, M.J. Brett, Investigation of thin sputtered Mn films for electrochemical

capacitors, Electrochim. Acta. 49 (2004) 4439–4446.

https://doi.org/10.1016/j.electacta.2004.04.035.

[38] K. Ogle, M. Mokaddem, P. Volovitch, Atomic emission spectroelectrochemistry applied to dealloying phenomena II. Selective dissolution of iron and chromium during active-passive cycles of an austenitic stainless steel, Electrochim. Acta. 55 (2010) 913–921. https://doi.org/10.1016/j.electacta.2009.08.028.

[39] F. Marchini, E.J. Calvo, F.J. Williams, Effect of the electrode potential on the surface composition and crystal structure of $LiMn_2O_4$ in aqueous solutions, Electrochim. Acta. 269 (2018) 706–713. https://doi.org/10.1016/j.electacta.2018.02.108.

[40] M. Baumung, L. Kollenbach, L. Xi, M. Risch, Undesired Bulk Oxidation of $LiMn_2O_4$ Increases Overpotential of Electrocatalytic Water Oxidation in Lithium Hydroxide Electrolytes, ChemPhysChem. (2019). https://doi.org/10.1002/cphc.201900601.

[41] J.C. Hunter, Preparation of a new crystal form of manganese dioxide: λ-MnO_2, J. Solid State Chem. 39 (1981) 142–147. https://doi.org/10.1016/0022-4596(81)90323-6.

[42] R. Benedek, M.M. Thackeray, A. Van De Walle, Pourbaix-like phase diagram for lithium manganese spinels in acid, J. Mater. Chem. 20 (2010) 369–374. https://doi.org/10.1039/b913226k.

[43] K. Takahashi, M. Saitoh, N. Asakura, T. Hibino, M. Sano, M. Fujita, K. Kifune, Electrochemical properties of lithium manganese oxides with differnt surface areas for lithium ion batteries, J. Power Sources. 136 (2004) 115–121. https://doi.org/10.1016/j.jpowsour.2004.05.014.

[44] Y. Shilina, B. Ziv, A. Meir, A. Banerjee, S. Ruthstein, S. Luski, D. Aurbach, I.C. Halalay, Combined Electron Paramagnetic Resonance and Atomic Absorption Spectroscopy/Inductively Coupled Plasma Analysis As Diagnostics for Soluble Manganese Species from Mn-Based Positive Electrode Materials in Li-ion Cells, Anal. Chem. 88 (2016) 4440–4447. https://doi.org/10.1021/acs.analchem.6b00204.

[45] R. Benedek, Role of Disproportionation in the Dissolution of Mn from Lithium

Manganate Spinel, J. Phys. Chem. C. 121 (2017) 22049–22053.

https://doi.org/10.1021/acs.jpcc.7b05940.

[46] L.-F. Wang, C.-C. Ou, K.A. Striebel, J.-S. Chen, Study of Mn Dissolution from

LiMn[sub 2]O[sub 4] Spinel Electrodes Using Rotating Ring-Disk Collection

Experiments, J. Electrochem. Soc. 150 (2003) A905.

https://doi.org/10.1149/1.1577543.

[47] L.F. Wang, B.J. Fang, J.S. Chen, Rotating ring-disc electrode measurements of

manganese dissolution and capacity loss of Li1+xMn2-xO4 and Li 1+xAlyMn2-x-yO4

spinel electrodes for lithium-ion batteries, J. Power Sources. 150 (2005) 1–10.

https://doi.org/10.1016/j.jpowsour.2005.01.043.

[48] D. Tang, Y. Sun, Z. Yang, L. Ben, L. Gu, X. Huang, Surface structure evolution of

LiMn2O4 cathode material upon charge/discharge, Chem. Mater. 26 (2014) 3535–

3543. https://doi.org/10.1021/cm501125e.

[49] T. Liu, A. Dai, J. Lu, Y. Yuan, Y. Xiao, L. Yu, M. Li, J. Gim, L. Ma, J. Liu, C. Zhan,

L. Li, J. Zheng, Y. Ren, T. Wu, R. Shahbazian-Yassar, J. Wen, F. Pan, K. Amine,

Correlation between manganese dissolution and dynamic phase stability in spinel-based

lithium-ion battery, Nat. Commun. 10 (2019) 1–11. https://doi.org/10.1038/s41467-

019-12626-3.

[50] D. Tang, L. Ben, Y. Sun, B. Chen, Z. Yang, L. Gu, X. Huang, Electrochemical

behavior and surface structural change of LiMn 2O4 charged to 5.1 v, J. Mater. Chem.

A. 2 (2014) 14519–14527. https://doi.org/10.1039/c4ta02109f.

[51] M.M. Thackeray, Y. Shao-Horn, A.J. Kahaian, K.D. Kepler, E. Skinner, J.T. Vaughey,

S.A. Hackney, Structural fatigue in spinel electrodes in high voltage (4 V)

Li/LixMn2O4 cells, Electrochem. Solid-State Lett. 1 (1998) 7–9.

https://doi.org/10.1149/1.1390617.

[52] Y.K. Lee, J. Park, W. Lu, A Comprehensive Experimental and Modeling Study on Dissolution in Li-Ion Batteries, J. Electrochem. Soc. 166 (2019) A1340–A1354. https://doi.org/10.1149/2.0111908jes.

[53] S.F.L. Mertens, G. Mészáros, T. Wandlowski, Dynamics of ionic liquid mediated quantised charging of monolayer-protected clusters, Phys. Chem. Chem. Phys. 12 (2010) 5417–5424. https://doi.org/10.1039/b921368f.

[54] R. Hendriks, D.M. Cunha, D.P. Singh, M. Huijben, Enhanced Lithium Transport by Control of Crystal Orientation in Spinel $LiMn_2O_4$ Thin Film Cathodes, ACS Appl. Energy Mater. 1 (2018) 7046–7051. https://doi.org/10.1021/acsaem.8b01477.

[55] S.F.L. Mertens, A. Hemmi, S. Muff, O. Gröning, S. De Feyter, J. Osterwalder, T. Greber, Switching stiction and adhesion of a liquid on a solid, Nature 534 (2016) 676–679. https://doi.org/10.1038/nature18275.